2021 IEEE International Conference on Robotics and Automation (ICRA 2021)
May 31 - June 4, 2021, Xi'an, China

2021 IEEE International Conference on Robotics and Automation (ICRA) | 978-1-7281-9077-8/21/$31.00 ©2021 IEEE | DOI: 10.1109/ICRA48506.2021.9560927

Reinforcement Learning Control of A Novel Magnetic Actuated Flexible-joint Robotic Camera System for Single Incision Laparoscopic Surgery

Dong Xu[1,†], Yuanlin Zhang[1], Wenshuai Tan[2], Hongxing Wei[2]

***Abstract*— This paper describes the control of a novel Magnetic Actuated Flexible-joint Robotic Surgical (MAFRS) camera system with four degrees of freedom (4-DOF) for single incision laparoscopic surgery. Based on the idea of motion decoupling, we designed a novel MAFRS system which is consists of an external driving device and a motor-free insertable wireless robotic device with a hollow flexible joint. Due to the problems of abdominal wall obstruction and variability in abdominal wall thickness during the actual application of the MAFRS system, as well as the existence of multiple permanent magnets and magnetically conductive media, high-precision position and attitude control of the insertable device without onboard motors has always been a challenge. We use the external driving device to generate a magnetic field to control the position and attitude of the internal robotic device. Aiming at the automatic precise tilt motion control of the novel MAFRS camera system, we have developed a closed-loop control scheme using the Deep Deterministic Policy Gradient (DDPG) algorithm. By referring to the damping characteristics of human muscles, a virtual-muscle method is proposed to eliminate the chattering problem of the MAFRS camera at specific angles. The experimental investigations indicate that the internal robotic device can be effectively controlled under different abdominal wall thicknesses. The tilt motion control accuracy is within 0.5°, and it has good adaptability and anti-interference performance.**

I. INTRODUCTION

Traditional open abdominal surgery is performed through a large incision (usually about 10 centimeters) so that the area being operated on is in direct view. This is effective, but the disadvantages are also obvious, such as longer recovery time and large cosmetic defects[1]. The development of techniques within Single Incision Laparoscopic Surgery (SILS) allows surgeons to perform procedures through one small incision[2], thereby offering benefits to the patients including reduced trauma, quicker recovery and reduced potential of surgical complications. However, the problems of visual occlusion and instrument interference due to the multiple surgical instruments shared a single incision limit the development of SILS. The use of robotics attempts to alleviate these constraints and further advance SILS[3], [4].

*This research was supported by the National Nature Science Foundation of China (under Grant No. 61673031)

†Corresponding Author: xd@buaa.edu.cn(Dong Xu)

[1]School of Automation Science and Electrical Engineering, Beihang University, No.37 Xueyuan Road, Beijing 100191, China {xd,zyl}@buaa.edu.cn

[2]School of Mechanical Engineering and Automation, Beihang University, No.37 Xueyuan Road, Beijing 100191, China sebastian_tan@163.com,weihongxing@buaa.edu.cn

In recent years, to solve the above-mentioned problems, more and more research teams begin to consider putting the camera device into the abdominal cavity, away from the surgical incision and using a magnetic field to fix and control the camera system. Insertable cameras with magnetic fixation and positioning for laparoscopic procedures have been reported in [5], [6]. In these solutions, the magnetic elements are intended to fix the camera device. Manipulation of the camera devices for positioning and orientation adjustments is normally achieved by manually maneuvering the external permanent magnets.

To improve the translational function in addition to anchoring for a robotic laparoscopic camera, [7] introduces a camera based on a cantilever attachment mechanism, which uses a rigid ring and a cantilever bar to fix the magnetic camera next to the incision. A magnetic handle provides magnetic coupling with the internal permanent magnets is applied with two onboard motors for both pan and tilt motion control. The design in [8] replaces pan motion motors by using magnetic coupling between the external handles and onboard permanent magnets to achieve manually actuated pan motion. However, one onboard motor still has to be reserved for tilt motion control in these designs. Obviously, the onboard motors require not only complex peripheral mechanisms that result in bulky articulated designs, but also consume extra onboard power, thereby reducing the working time of wireless camera devices.

In order to completely eliminate the onboard motor and the need for articulated design, Xiaolong Liu et al. [9] proposed a motor-free active locomotion mechanism for a laparoscopic camera. The mechanism uses coils to generate a 3D rotating magnetic field, thereby generates both torque to rotate the inside rotor dome in all three dimensions, and force to serve as an anchoring system that keeps the camera steady during a surgical procedure. However, the magnetic force and torque will rapidly reduce while the distance from the rotor to the stator increases. Therefore, the disadvantages of this solution include weak load capacity, short effective control distance and coils' overheating. Later, Xiaolong Liu et al. proposed a new compact insertable camera robot and designed a control system for the new camera robot[10], [11]. The camera they designed is always close to the abdominal wall, which causes camera lens' contamination easily. At the same time, its control system relies on the analysis of the thickness of the abdominal wall, which is obviously inconvenient in practical use, and the patient's abdominal

Authorized licensed use limited to: Chungbuk National Univ. Downloaded on May 08,2024 at 01:14:14 UTC from IEEE Xplore. Restrictions apply.

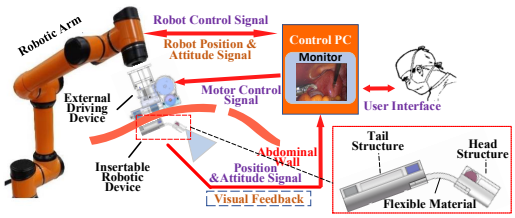

Fig. 1. Conceptual illustration of the MAFRS camera system.

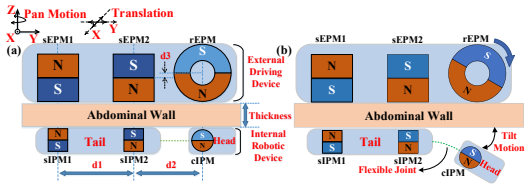

Fig. 2. Working principle of the MAFRS camera system. In the figure, N and S represent the N and S poles of the permanent magnets, $d1$ represents the distance between the center axes of two square permanent magnets, $d2$ represents the distance between the center axes of cylindrical permanent magnet and the adjacent square permanent magnet and $d3$ represents the deviation of sEPM2 and rEPM along the Z-axis.

wall is not strictly a plane. The modeling results may need to be modified according to the situation of different patients, so the camera system has poor versatility. There is a need to develop a magnetic actuated robotic surgery camera system with a simple structure and convenient to control. At the same time, the system should have good adaptability and anti-interference performance.

In this paper, we introduce our MAFRS system and propose a control algorithm based on this MAFRS system, as is conceptually illustrated in Fig. 1. The MAFRS camera system design features a motor-free actuation mechanism for anchoring, navigating, and tilting the internal robotic device by externally generated magnetic field. The key idea and novelty of the actuation mechanism design is to decouple the translation, pan motion and tilt motion of the internal robotic device. Meanwhile, the structure of the internal device adopts a segmented design and uses a hollow flexible joint instead of a hinged structure. To the knowledge of the authors, this paper is the first design using a hollow flexible joint to implement tilt motion. This design not only has a simple structure, but also reduces the control difficulty of the MAFRS camera system. The hollow design provides an excellent way for power supply and data transmission.

The contributions of this paper include: 1) a novel Magnetic Actuated Flexible-joint Robotic Surgery (MAFRS) camera system is introduced; 2) a controller based on deep reinforcement learning is proposed for the tilt motion control of the MAFRS camera system; 3) a virtual-muscle method to eliminate the chattering of the MAFRS camera at specific angles is proposed; and 4) a fabricated dummy MAFRS camera system is demonstrated, and experimental analysis is conducted for evaluating the control accuracy of the MAFRS camera system.

II. DESCRIPTION OF CAMERA SYSTEM STRUCTURE

The working principle of the MAFRS camera system is illustrated in Fig. 2. The magnetic actuation mechanism consists of (i) an external driving device with two square external permanent magnets (sEPMs) and a ring-shaped external permanent magnet (rEPM), and (ii) an internal robotic device with two square internal permanent magnets (sIPMs) and a cylindrical internal permanent magnet (cIPM). The driving device is positioned externally against abdominal wall and the robotic device is pushed against abdominal wall internally. When the driving device is directly above the internal robotic device, the magnetic poles of the permanent magnets in the internal magnetic circuit are opposite the poles of the permanent magnets in the external driving magnetic circuit. The distribution of the magnetic poles of each permanent magnet is shown in Fig. 2. This magnetic pole distribution mode can ensure that no repulsive force will be generated to sIPM2 when the rEPM rotates clockwise within a certain range, which is conducive to ensuring the gravity compensation of the internal device by the external driving device.

This mechanism is designed to enable translation, pan motion, and tilt motion, in addition to the compensation of the gravity of the internal robotic device (fixation). This structural design decouples each movement; the internal robotic device's translation is provided by moving the external driving device along the dermal surface with the attractive force between the EPMs and the IPMs. A spinning motion of the external driving device along the Z-axis can actuate the head's pan motion by the coupled magnetic field of the EPMs and the IPMs. As is shown in Fig. 2(b), the internal robotic device's head and tail are connected by the hollow flexible joint, so the rEPM of the external driving device can be rotated to actuate the tilt motion of the internal robotic device's head. Adopting such an innovative structural design avoids using onboard motors and electromagnetic coils, thereby solving various defects of existing solutions. Simultaneously, the camera (embedded in the internal robotic device's head) will be suspended in midair, effectively preventing the lens from contacting the abdominal wall and contaminating the lens.

An attitude sensor (MPU6050) is embedded in the robotic device's head to acquire tilt angles. A lithium battery, voltage regulator module (AMS1117) and a wireless transceiver (CC2450) are embedded in the tail of the internal robotic device. The hollow flexible joint can not only realize a smooth bending of the robotic device's head, but also provide an excellent way for the power supply and data transmission of the modules working in the head cavity.

III. CONTROL METHOD OF MAGNETIC ACTUATION MECHANISM

Our previous research [12] has been verified that the magnetic coupling of the internal and external devices can provide sufficient anchoring and driving force, and the rationality and feasibility of the structural design have been

Authorized licensed use limited to: Chungbuk National Univ. Downloaded on May 08,2024 at 01:14:14 UTC from IEEE Xplore. Restrictions apply.

verified. However, after the internal robotic device is moved to a surgical position, high-precision control of the tilt motion is required to accurately control the attitude of the internal robotic device.

A. Translation and Pan Motion Control

With this structural design, the external driving device is small and compact; we can easily mount the external driving device on the high-precision robotic arm (AUBO-i5). The MAFRS camera system's control program integrates the control program of the robotic arm. The external driving device's attitude adjustment can be realized by controlling the robotic arm, thereby controlling the translation and pan motion of the internal robotic device. The positioning accuracy of the robotic arm's endpoint can reach $0.02\mathrm{mm}$, enough to meet the fine adjustment of the external driving device's attitude.

B. Tilt Motion Control

Based on the existing prototype, the corresponding relationship between the rotation angle of rEPM and the head's tilt angle can be obtained, as is shown in Fig. 3. The distance between the internal and external devices of the MAFRS camera system is $30\mathrm{mm}$. Changes in the patients' abdominal wall thickness will have a large impact on the curve's shape. It is not easy to accurately describe the corresponding relationship in the form of mathematical expressions. Therefore, we have proposed a novel closed-loop autonomous control framework for the MAFRS camera system's tilt motion based on the Deep Deterministic Policy Gradient (DDPG) algorithm, a model-free gradient algorithm. Fig. 4 shows a schematic diagram of the structure of the DDPG algorithm used in this work. There are two feed-forward neural networks, namely, the actor network and the critic network. Each of the networks is composed of four layers with 500, 200, 10, and 1 node. For details of the DDPG algorithm, see Algorithm 1.

In reinforcement learning, the design of the components of the Markov decision process is one of the most crucial processes. The performance of the algorithm and the speed of the convergence are strongly affected by the correctness of the state space, action space, and reward function[13]. In this work, the reinforcement learning-based controller's

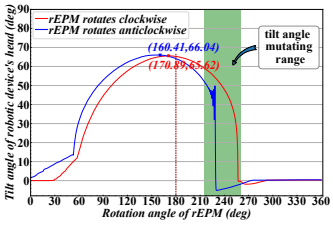

Fig. 3. The corresponding relationship between the rotation angle of the rEPM and the tilt angle of the internal robotic device. The distance between the external driving device and the internal robotic device is $30\mathrm{mm}$. The rEPM rotates 360° clockwise and then rotates 360° anticlockwise. The range marked in green is the range where the rEPM rotates a small angle, but the tilt angle of the internal robotic device's head changes rapidly.

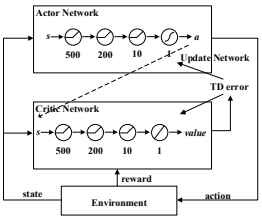

Fig. 4. Schematic diagram of the structure of the control policy networks

primary goal is to keep the internal robotic device's head at the expected angle. Since the head's current tilt angle can be obtained from the attitude sensor and rEPM is driven by a stepping motor, the state space $s \in \sum(s)$ is defined as (5), and the action space $a \in \sum(a)$ is defined as (6). From Fig. 3, we can see that within a specific angle range, a small change of the rEPM may lead to a rapid change of the tilt angle, which is undesirable. Also, when the angle deviation is small, we hope that the action chosen by the agent should not be too large. Therefore, the reward function is defined as (7).

$$\sum(s) = \{y_e/y_{emax}, wy, flag\}, \tag{5}$$

where y_e is the difference between the expected angle of the internal robotic device's head and the current angle, y_{emax} is the maximum difference, and wy is the angular velocity of the head. In addition, $flag$ indicates whether the y_e is within 1°. If the y_e is less than 1°, the $flag = 1$, otherwise the $flag = 0$. In this work, we set $y_{emax} = 70$.

$$\sum(a) = \{\gamma_a\}, \tag{6}$$

where γ_a is the control command of the stepping motor.

$$r = \begin{cases} -\left(|y_e/y_{emax}| + k_a\alpha_a^2 + k_c y_c^2\right), & |y_e| > 1^\circ \\ -\left(|y_e/y_{emax}| + k_a\alpha_a^2 + k_c y_c^2\right) + r_g, & |y_e| \le 1^\circ \end{cases}, \tag{7}$$

where α_a is the action selected by the agent, y_c represents the change of the tilt angle after the agent cycles for one step, r_g is a constant, represents the extra reward when the deviation between the real-time angle and the expected angle is less than 1°, k_a and k_c are constant coefficients. The k_a and k_c determine the impact of their corresponding items on the reward function. In this work, through the experiments, we set $k_a = 0.03$, $k_c = 0.001$, and $r_g = 3$.

In addition, during the action exploration process, the exploration policy μ' is designed by adding a random decaying noise ξ as (8)

$$\mu'(s_j) = \mu\left(s_j|\theta_j^\mu\right) + \xi_j, \tag{8}$$

where $\xi_j = r_d * \xi_{j-1}$, with r_d as a decay rate.

C. Eliminate the Chattering by Virtual-muscle Method

Since the real physical control tasks have continuous (real-valued) and high-dimensional action spaces, it is impossible to traverse all states and all actions within a limited time. Therefore, in certain specific states, the agent may tend to periodically change its action, which is called the chattering

Authorized licensed use limited to: Chungbuk National Univ. Downloaded on May 08,2024 at 01:14:14 UTC from IEEE Xplore. Restrictions apply.

Algorithm 1 Deterministic Deterministic Policy Gradient (DDPG) algorithm

Initialize critic network $Q\left(s,a|\theta^{Q}\right)$ and actor network $\mu\left(s|\theta^{\mu}\right)$ with random weights θ^{Q} and θ^{μ};
Initialize target network Q' and μ' with weights $\theta^{Q'} \leftarrow \theta^{Q}$, $\theta^{\mu'} \leftarrow \theta^{\mu}$;
Initialize replay memory Buffer: $\mathbf{R}$;
Initialize noise parameters ξ_1;
for episode = 1 to M , **do**
    Observe the initial state of MAFRS camera: s_1;
    for t = 1 to T , **do**
        Select action $a_t = \mu\left(s_t|\theta^{\mu}\right) + \xi_t$ based on the current policy and noise ξ_t;
        Perform the action a_t and observe the new state s_{t+1} and reward r_t;
        Store transition (s_t, a_t, r_t, s_{t+1}) in $\mathbf{R}$;
        Sample a random minibatch of N transitions (s_i, a_i, r_i, s_{i+1}) from $\mathbf{R}$;
        Set $y_i = r_i + \gamma Q'\left(s_{i+1}, \mu'\left(s_{i+1}|\theta^{\mu'}\right)|\theta^{Q'}\right)$;
        Update critic network by minimizing the loss function
        $L = \frac{1}{N}\sum_i \left(y_i - Q\left(s_i, a_i|\theta^{Q}\right)\right)^2$
        Update the actor policy using the sampled gradient
        $\nabla_{\theta^{\mu}} J \approx \frac{1}{N}\sum_i \nabla_a Q\left(s,a|\theta^{Q}\right)\big|_{s=s_i,a=\mu(s_i)} \nabla_{\theta^{\mu}}\mu\left(s|\theta^{\mu}\right)\big|_{s_i}$
        Update the target networks
        $\theta^{Q'} \leftarrow \tau\theta^{Q} + (1-\tau)\theta^{Q'}$
        $\theta^{\mu'} \leftarrow \tau\theta^{\mu} + (1-\tau)\theta^{\mu'}$
    end for
end for

phenomenon[14]. Besides, it can be seen from Fig. 3 that when the rEPM rotates to a certain angle range, a small change of the rEPM may cause a rapid change of the head's tilt angle, which may aggravate the chattering phenomenon even cause fail to converge to the expected angle.

To solve this problem, we use the virtual-muscle method to eliminate possible chattering. In our previous research [15], we know that the muscle spindle, as a receptor of motion feedback, has an important effect on the good performance of neuromuscular system. It makes the system express low viscosity at a high velocity but transfer into high viscosity at a low velocity. This makes the relationship between the input and output of the system approximately bell-shaped. Inspired by the characteristics of human muscle, and for the convenience of control, we constructed a bell-shaped function as shown in (9) to simulate the characteristics of human muscle. We adjust the action value given by the DDPG-based agent according to (9), (10), and (11). In this way, the system has a high viscosity when the tilt angle deviation is small and a low viscosity when the tilt angle deviation is large, which perfectly simulates the characteristics of human muscles.

$$y_a = \frac{-k_1}{\sqrt{2\pi}\sigma}\left[\exp\left(-\frac{(x-\mu)^2}{2\sigma^2}\right) - k_2\right] + k_d, \tag{9}$$

$$\gamma_d = \begin{cases} y_a, & y_a \le 1 \\ 1, & y_a > 1 \end{cases}, \tag{10}$$

$$\alpha_a = \alpha_a * \gamma_d, \tag{11}$$

where x represents the real-time angle value, μ represents the expected angle, k_1, k_2, k_d and σ are constant. k_1, k_2 and σ determines the shape of the bell-shaped curve, and k_d is to prevent the action value from being too small so that the driving motor cannot work normally. In this work, through the experiments, we set $k_1 = 12$, $k_2 = 1$, $\sigma = 6$, and $k_d = 0.1$.

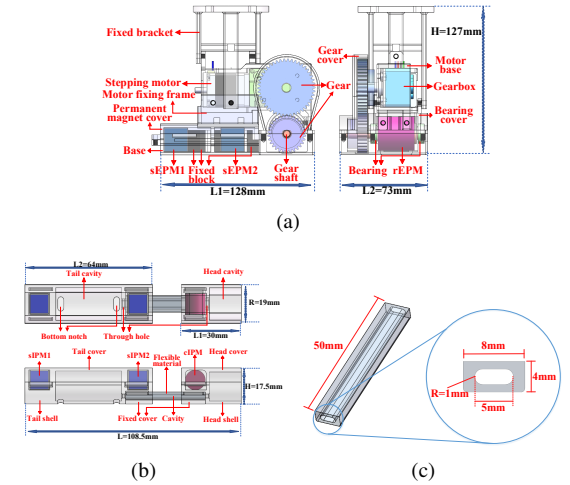

Fig. 5. (a) External driving device structure. (b) Internal robotic device structure. (c) Structural dimensions of the flexible joint.

IV. PROTOTYPE DEVELOPMENT AND EXPERIMENTAL INVESTIGATION

A. Experimental Platform

Fig. 1 shows the overview of the experimental platform and Fig. 5 shows the details of the key structure of the MAFRS camera system. The prototype system uses the AUBO-i5 light collaborative robotic arm, and uses a 25mm

Authorized licensed use limited to: Chungbuk National Univ. Downloaded on May 08,2024 at 01:14:14 UTC from IEEE Xplore. Restrictions apply.

thick polypropylene board to simulate the thickness of the abdominal wall. The housings of the external driving device and the internal robotic device are made of low-viscosity photosensitive resin materials and made by 3D printing technology. At the same time, the flexible joint is made of silicone materials and made by 3D printing. The specific size parameters of the flexible joint used in this work are shown in Fig. 5(c).

An abdominal tissue thickness upon insufflation ranging from 20mm to 40mm was considered when selecting the permanent magnets for the MAFRS camera system. This range is representative of patients with a body mass index up to 30kg/m^2, thus including overweight population[16]. The specifications and spacing of the permanent magnets in Fig. 2 are shown in Table I, and all permanent magnets are made of NdFeB Grade N52.

B. Verification of Translation and Pan Motion

According to [17], the friction coefficient between the internal robotic device's housing and the abdominal wall of the human body is about 0.1, so we have roughened the upper surface of the internal robotic device to ensure that the friction coefficient between the polypropylene board and the internal robotic device is greater than 0.1. It is also assumed that the thickness of the abdominal wall is 30mm. As is shown in Fig. 6, in the initial state, the external driving device is placed directly above the internal robotic device. By controlling the translation and rotation movement of the end of the robotic arm, the translation and rotation of the external driving device can be driven, thereby driving the translation and pan motion of the internal robotic device. By taking the average of multiple measurements, it can be measured that in the experimental environment, the offset required for the translation of the internal robotic device and the deviation angle required for the pan motion are shown in Table II.

C. Verification of Tilt Motion

Based on our prototype, through the interaction with the real environment, the training experiment for DDPG-based agent was completed. In the experiments, we used the minibatch size of 32 for tasks and the soft replacement parameter τ and the discount factor γ are set to 0.01 and 0.9 respectively. The learning rates are 0.001, and the replay memory buffer size is 30000.

We evaluate the feasibility of our method in the 400 episodes learning tests, and every episode has 500 steps.

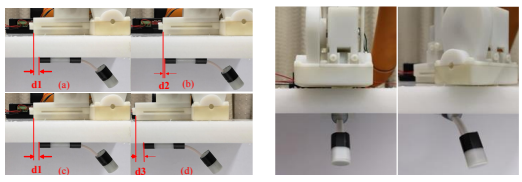

(a) (b)

Fig. 6. (a) Verification of translational motion along the Y-axis. (b) Verification of pan motion.

TABLE I

SPECIFICATIONS AND SPACING OF THE PERMANENT MAGNETS

sEPMs:		Square
	Size	$20\text{mm} \times 20\text{mm} \times 20\text{mm}$
sIPMs:		Square
	Size	$10\text{mm} \times 10\text{mm} \times 10\text{mm}$
rEPM:		ring-shaped, Diametrically magnetized
	Size	OD 28mm, ID 12mm, Height 30mm
cIPM:		Circular, Diametrically magnetized
	Size	Diameter 10mm, Height 8mm
d1:		40mm
d2:		40mm
d3:		4mm

TABLE II

OFFSET REQUIRED FOR TRANSLATION AND DEVIATION ANGLE REQUIRED FOR PAN MOTION

Direction of movement	Offset required for translation	Deviation angle required for pan motion
positive direction of X-axis	$9mm$	/
negative direction of X-axis	$9mm$	/
positive direction of Y-axis	$11mm$	/
negative direction of Y-axis	$5mm$	/
positive direction of Z-axis	/	$13°$
negative direction of Z-axis	/	$12°$

From Fig. 7(a), we can find that the network trained from scratch and converged to an almost constant step number value after 200 episodes, which means our method is effective. After about 3 hours and 400 episodes of training, the reward value has stabilized, which shows that the parameter selection is appropriate. Due to the exploration possibility, there are some small fluctuations in the curve. Meanwhile, it can be seen from Fig. 7(b) that the reward value for each episode is basically negative at the beginning. After sixty episodes, the reward value begins to rise rapidly, indicating that the DDPG-based agent has learned a better strategy. In the later stages of training, the agent can reach the expected angle with the minimum number of steps, so the cumulative reward value for each episode becomes low and tends to stabilize.

As is shown in Fig. 8(a), when the angle of the internal robotic device's head is tilted from $57°$ to $40°$, the robotic device's head will swing back and forth at the angle of $40°$. At the same time, it can be seen from Fig. 8(b) that after using our proposed virtual-muscle method can effectively eliminate the head's chattering.

The internal robotic device's head tilt motion control is tested under the thickness of the abdominal wall of 30mm and 40mm respectively. The experimental results are shown in Fig. 9(a) and Fig. 9(b). It can be seen from Fig. 9(a) and Fig. 9(b) that under different abdominal wall thicknesses, the agent can effectively control the tilt motion of the internal robotic device's head, and the control accuracy is within $0.5°$. When the thickness of abdominal wall is 40mm, the maximum tilt angle of internal robotic device's head is greater than $60°$, which can meet the needs of normal surgeries.

Authorized licensed use limited to: Chungbuk National Univ. Downloaded on May 08,2024 at 01:14:14 UTC from IEEE Xplore. Restrictions apply.

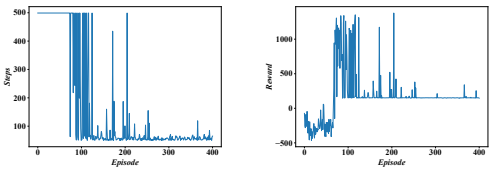

(a) (b)

Fig. 7. (a) Network converging curve. (b) The Learning curve for 400 training episodes.

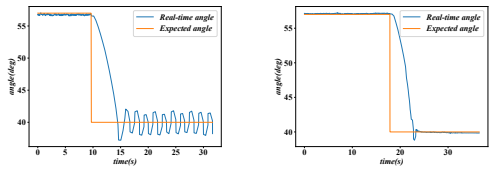

(a) (b)

Fig. 8. The angle of the internal robotic device's head is tilted from 57° to 40°. (a) Without using the virtual-muscle method to eliminate chattering (b)Using the virtual-muscle method to eliminate chattering.

When the tilt angle of the internal robotic device's head deviates from the expected angle due to external interference, the DDPG-based control system will automatically adjust the tilt angle to keep the internal robotic device's head at the expected angle, as is shown in Fig. 10.

V. CONCLUSION AND FUTURE WORK

In this paper, a closed-loop control system for a novel insertable laparoscopic camera, i.e. the MAFRS camera, has been presented to enable automatic precise control. The experimental results indicate that the MAFRS camera control system can effectively control the internal robotic device, and the tilt motion control accuracy is within 0.5°. The proposed virtual-muscle method can effectively eliminate the chattering of the internal robotic device's head at specific angles. In our future work, closed-loop control of translation and pan motion will be realized, and the image information collected by the camera will be used as feedback to further improve the control accuracy in the future. Furthermore, the MAFRS camera system will also be tested in vivo using a pig's abdominal cavity.

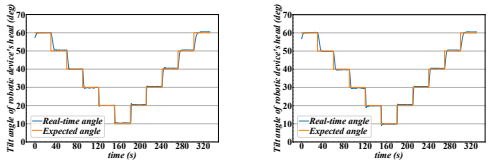

(a) (b)

Fig. 9. (a) The thickness of the abdominal wall is 30mm, and the expected tilt angle of the head follows the sequence 60°, 50°, 40°, 30°, 20°, 10°, 20°, 30°, 40°, 50°, 60°. (b) The thickness of the abdominal wall is 40mm, and the expected tilt angle of the head follows the sequence 60°, 50°, 40°, 30°, 20°, 10°, 20°, 30°, 40°, 50°, 60°.

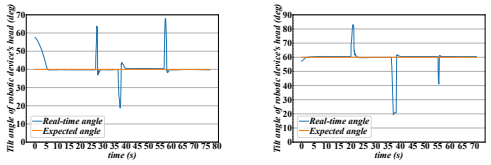

(a) (b)

Fig. 10. Simulate interference such as the collision of surgical instruments that causes the angle to change rapidly and return to the expected angle curve; (a) expected angle is 40°; (b) expected angle is 60°.

REFERENCES

[1] Richardson, W. S., Carter, K. M., Fuhrman, G. M., Bolton, J. S., & Bowen, J. C. (2000). Minimally invasive abdominal surgery. Ochsner Journal, 2(3), 153-157.

[2] Romanelli, J. R. , & Earle, D. B. . (2009). Single-port laparoscopic surgery: an overview. Surgical Endoscopy, 23(7), 1419-1427.

[3] Lehman, A. C. , Rentschler, M. E. , Farritor, S. M. , & Oleynikov, D. . (2007). The current state of miniature in vivo laparoscopic robotics. Journal of Robotic Surgery, 1(1), 45-49.

[4] Leong, F. , Garbin, N. , Di Natali, C. , Mohammadi, A. , Thiruchelvam, D. , & Oetomo, D. , et al. (2016). Magnetic surgical instruments for robotic abdominal surgery. IEEE Reviews in Biomedical Engineering, 1-1.

[5] Swain, P. , Austin, R. , Bally, K. , & Trusty, R. . (2010). Development and testing of a tethered, independent camera for notes and single-site laparoscopic procedures. Surgical Endoscopy, 24(8), 2013-2021.

[6] Cadeddu, J. , Fernandez, R. , Desai, M. , Bergs, R. , Tracy, C. , & Tang, S. J. , et al. (2009). Novel magnetically guided intra-abdominal camera to facilitate laparoendoscopic single-site surgery: initial human experience. Surgical Endoscopy, 23(8), 1894-1899.

[7] Terry, B. S. , Mills, Z. C. , Schoen, J. A. , & Rentschler, M. E. . (2012). Single-port-access surgery with a novel magnet camera system. IEEE Transactions on Biomedical Engineering, 59(4), 1187-1193.

[8] Simi, M. , Ciuti, G. , Tognarelli, S. , & Valdastri, P. . (2010). Magnetic link design for a robotic laparoscopic camera. Journal of Applied Physics, 107(9), 95.

[9] Liu, X. , Mancini, G. J. , & Tan, J. . (2014). Design of a unified active locomotion mechanism for a capsule-shaped laparoscopic camera system. Proceedings - IEEE International Conference on Robotics and Automation. IEEE.

[10] Liu, X. , Mancini, G. J. , & Tan, J. . (2015). Design and analysis of a magnetic actuated capsule camera robot for single incision laparoscopic surgery. 2015 IEEE/RSJ International Conference on Intelligent Robots and Systems (IROS). IEEE.

[11] Liu, X. , Yazdanpanah, A. R. , Mancini, G. J. , & Tan, J. . (2015). Control of a Magnetic Actuated Robotic Surgical camera system for single incision laparoscopic surgery. 2015 IEEE International Conference on Robotics and Biomimetics (ROBIO). IEEE.

[12] Xu, D. , Zhang, Y. , Tan, W. , Wei, H. , & Xu, P. . (2020). Design and Implementation of A Magnetic Actuated Capsule Camera Robot System for Single Incision Laparoscopic Surgery. 2020 IEEE 18th International Conference on Industrial Informatics (INDIN). IEEE.

[13] Liu, W. , Jing, Z. , D'Eleuterio, G. , Chen, W. , Yang T. , & Pan, H. . (2019). Shape Memory Alloy Driven Soft Robot Design and Position Control Using Continuous Reinforcement Learning. 2019 2nd International Conference on Intelligent Autonomous Systems (ICoIAS). IEEE

[14] Lillicrap, T. P., Hunt, J. J., Pritzel, A., Heess, N., Erez, T., Tassa, Y., ... & Wierstra, D. (2015). Continuous control with deep reinforcement learning. arXiv preprint arXiv:1509.02971.

[15] Xu, D. , Zhang, S. , & Wei, H. . (2015). Virtual musculoskeletal control model with a spindle-like fuzzy algorithm for robotic compliance. Applied Mathematical Modelling, 39(12), 3265-3279.

[16] Best, S. L. , Bergs, R. , Gedeon, M. , Paramo, J. , Fernandez, R. , & Cadeddu, J. A. , et al. (2011). Maximizing coupling strength of magnetically anchored surgical instruments: how thick can we go?. Surgical Endoscopy, 25(1), 153-159.

[17] Loring, S. H. , Brown, R. E. , Gouldstone, A. , & Butler, J. P. . (2005). Lubrication regimes in mesothelial sliding. Journal of Biomechanics, 38(12), 2390-2396.

Authorized licensed use limited to: Chungbuk National Univ. Downloaded on May 08,2024 at 01:14:14 UTC from IEEE Xplore. Restrictions apply.